Photochemical & Photobiological Sciences

PAPER

Cite this: *Photochem. Photobiol. Sci.*, 2018, **17**, 1429

Ternary semiconductor $Zn_xAg_{1-x}S$ nanocomposites for efficient photocatalytic degradation of organophosphorus pesticides†

Dasari Ayodhya * and Guttena Veerabhadram

The construction of ternary semiconductor nanostructures has attracted much attention in photocatalysis by virtue of their tunable elemental composition and band structure. Here, ternary semiconductor $Zn_xAg_{1-x}S$ ($0 \leq x \leq 1$) composites were successfully prepared by a simple and low-cost hydrothermal method without using any surfactant. Combined analyses using XRD, N_2 sorption, SEM, TEM and UV-vis DRS revealed that the ternary composite semiconductor materials exhibited well-developed crystalline frameworks, large surface areas of 15–70 $m^2\ g^{-1}$, sizes of 10–30 nm, and outstanding UV light absorption properties. Data from XRD and TEM indicate that photocatalysis might contribute to the formation of the strong interfacial interaction between ZnS and Ag_2S nanoparticles. The photocatalytic activities were investigated *via* the degradation of organophosphorus pesticides, including malathion (MLT), monocrotophos (MCP) and chlorpyrifos (CPS), using the $Zn_xAg_{1-x}S$ composites under UV light irradiation. The toxicity of MLT, MCP, and CPS was reduced by photocatalysis and photolysis; however, photocatalysis had a greater impact. Superior photocatalytic performance was exhibited by the $Zn_{0.5}Ag_{0.5}S$ catalyst owing to its large surface area and the presence of Ag^0 with improved charge transfer in comparison with that of bare ZnS and Ag_2S. Assays of stability and reusability indicated that the $Zn_{0.5}Ag_{0.5}S$ composite retained more than 85% of its activity after five cycles of use. On the basis of the results, a possible photocatalytic mechanism of the prepared samples was proposed. This study indicates a potential application of the ternary semiconductor materials in the efficient UV light-driven photocatalytic degradation of other pollutants that may cause environmental pollution.

Received 30th May 2018,
Accepted 10th September 2018

DOI: 10.1039/c8pp00220g

rsc.li/pps

Introduction

The release of toxic and persistent organic pollutants into aquatic environments has been a growing concern in the recent past, and addressing the issue of their remediation is considered to be an urgent need. Hazardous organic pollutants such as pesticides, polychlorinated biphenyls, halogenated organic solvents and polycyclic aromatic hydrocarbons are discharged from industrial and wastewater treatment plants and are responsible for contamination of ground and surface water.[1,2] Pesticides in aquatic environments are potentially toxic and are difficult to decompose by conventional treatment processes. The search for new methodologies to promote the photodecomposition of organophosphorus pesticides is of major relevance for the elimination of pollution in a variety of environmental situations. Common methods for eliminating pollution from aqueous solutions include adsorption, biological processes, ozonation, photolysis, Fenton reactions, and membrane processes, of which each has its own advantages and disadvantages. One advanced method of oxidation is photocatalysis, which is a process based on the absorption of light energy by nanoparticles.[3] This process using nanoparticles as a catalyst involves the production of hydroxyl radicals ($HO^{\bullet}$), which can be generated from hydrogen peroxide (H_2O_2), ozone or oxidants, in combination with the use of ultraviolet (UV) radiation for achieving complete degradation or mineralization of organic pollutants into CO_2 and H_2O. Catalysts such as semiconductor nanostructures

Department of Chemistry, Osmania University, Hyderabad-500007, Telangana state, India. E-mail: ayodhyadasari@gmail.com; Tel: +91-9010877323

† Electronic supplementary information (ESI) available: The photocatalytic degradation of the organophosphorus pesticides, namely, MLT, MCP and CPS, was monitored using UV-visible absorption spectra in the absence and presence of the $Zn_xAg_{1-x}S$ catalyst, which are shown in Fig. S1(a–c) and S2(a–c), respectively. The effects of the addition of different scavengers on the photocatalytic degradation of (a) MLT, (b) MCP and (c) CPS by the ZnS and Ag_2S nanocomposites, respectively (Fig. S3 and S4). Cycling runs in the photocatalytic degradation of (a) MLT, (b) MCP and (c) CPS in the presence of the synthesized ZnS and Ag_2S nanocomposites under UV light irradiation, respectively (Fig. S5 and S6). See DOI: 10.1039/c8pp00220g

have been used for photocatalytic oxidation of pollutants present in water.[4–8]

In recent years, researchers have focused on semiconductor photocatalysis owing to its potential applications in energy conversion and degradation of environmental pollutants.[9–12] Reported photocatalyst systems, to the best of our knowledge, can be generally classified into oxides,[10,12–15] sulfides,[16–18] oxysulfides,[19] nitrides,[20] and oxynitrides.[21] However, all current photocatalysts can only be activated under ultraviolet or visible light irradiation and thus do not work when a light source is not present. Recently, the great potential of semiconductor photocatalysis for resolving environmental pollution and energy shortages has been widely recognized.[22,23] Numerous efforts have been made to develop efficient photocatalysts. Many new materials, such as $Bi/BiVO_4$,[24] $g\text{-}C_3N_4/SmVO_4$,[25] $Sr_{0.25}Bi_{0.75}O_{1.36}$,[26] $CeO_2/SnO_2/rGO$,[27] and Ag_3PO_4,[28] with photocatalytic activities within the visible light spectrum have been reported. However, drawbacks such as limited harvesting of visible light, rapid charge recombination and poor stability still hinder their applications. Therefore, the search for new methodologies to promote the photodecomposition of organic compounds such as dyes, phenols, and pesticides is of major relevance for the elimination of pollutants in a variety of environmental situations. Hence, new photocatalysts must be developed to overcome the shortcomings of conventional photocatalysts.

Among all the studied semiconductors, metal sulfides have exhibited the most promising activities in the treatment of water under UV light because of their suitable band energies. II–VI semiconductor compounds are of considerable interest because of their potential utility in a wide range of optoelectronic devices, high absorption coefficients, high efficiency of radiative recombination and band gaps that nearly match the visible region of the solar spectrum.[29–33] In particular, ZnS is a well-known photocatalyst as a result of the rapid generation of electron–hole pairs by photoexcitation and the high negative potentials of excited electrons and exhibits high activity in H_2 evolution, even without the assistance of noble metal cocatalysts.[34–36] However, the band gap of ZnS (3.66 eV) is too large for a visible light response,[35] and many methods, such as doping with noble metal ions,[37–39] the preparation of binary or ternary compounds and combination with various narrow-band-gap semiconductors, have been employed to endow ZnS with UV light activity.[40] Ternary semiconductor materials have been well studied because their optical band gaps are tunable by changing their compositions.[41] For instance, $Zn_xAg_{1-x}S$ has the potential to form a continuous series of ternary semiconductors and opens the possibility of varying the optical band gap systematically in a controlled way from the visible (Ag_2S = 1.3 eV) to the UV (ZnS = 3.66 eV) region. In recent years, doped ZnS systems such as Au–ZnS, Ag–ZnS and $Ag–ZnGeS_4$ hybrid nanostructures have also received special attention in photocatalysis for achieving enhanced photocatalytic activities in comparison with that of bare ZnS. More interestingly, the band gap width and band edge position of $Zn_xAg_{1-x}S$ can be precisely tuned by varying the concentrations of Ag^+ and Zn^{2+} ions. Owing to the advantages of ZnS and Ag, much attention has been paid to Ag-doped or Ag-deposited ZnS composite systems. Extensive studies have continued to produce a variety of composite structures with better performance than their individual components. Gupta *et al.*[37] observed the enhanced photocatalytic activity of Ag–ZnS in comparison with that of ZnS nanostructures.

From the background literature, it has been found that few studies are available on the degradation of organophosphorus pesticides using ternary semiconductor nanostructures; therefore, the UV-light-activated photocatalytic degradation of pesticides using $Zn_xAg_{1-x}S$ composites is a promising task. The objective of this study was to develop ternary semiconductor $Zn_xAg_{1-x}S$ composites without the use of any surfactant using a simple hydrothermal method as photocatalysts for the degradation of MLT, MCP, and CPS under UV light irradiation. A comparative study of the photocatalytic degradation of MLT, MCP, and CPS in the presence of $Zn_{0.5}Ag_{0.5}S$ was specifically performed with bare ZnS and Ag_2S NPs, as silver was incorporated into the ZnS lattice to enhance its photocatalytic efficiency. The reusability of these catalysts was also determined using a cyclic degradation test. The reactive species involved in the photodegradation of pesticides were determined, as well as the rate of the photochemical reaction, and a possible mechanism of the enhanced performance of $Zn_xAg_{1-x}S$ was also proposed. The structure, morphology, surface composition and chemical status of elements in the as-prepared $Zn_xAg_{1-x}S$ composites were characterized by UV-vis DRS, PL, XRD, SEM, TEM, BET measurements, and XPS.

Experimental section

Materials and methods

All starting materials were commercially available and were used as received without further purification. Silver nitrate ($AgNO_3$), zinc nitrate tetrahydrate ($Zn(NO_3)_2{\cdot}4H_2O$) and sodium sulfide ($Na_2S{\cdot}9H_2O$) were purchased from S.D. Fine Chemicals, Mumbai, India. Analytically pure malathion, monocrotophos and chlorpyrifos (97%) were purchased from Sigma-Aldrich (Bangalore Bonded Warehouse, India), and 100 mg L^{-1} solutions of the pesticides (malathion, chlorpyrifos, and monocrotophos) were prepared in double-distilled water and stored at 4 °C. All solutions and reaction mixtures were prepared using double-distilled water.

Synthesis of ternary $Zn_xAg_{1-x}S$ nanocomposites

A series of $Zn_xAg_{1-x}S$ (x = 0, 0.5 and 1.0) nanocomposites were prepared by a simple and low-cost hydrothermal method without using any capping agent. Different molar ratios of Zn/Ag (x = 0, 0.5, 1.0) were used in the preparation of the nanocomposites using various amounts of Zn^{2+}

($Zn(NO_3)_2{\cdot}4H_2O$; 0.5 mM), Ag^+ ($AgNO_3$; 0.05 mM) and S^{2-} ($Na_2S{\cdot}9H_2O$; 0.05 mM) precursors. Typically, different amounts of Zn^{2+} and Ag^+ were dissolved in 100 mL of double-distilled water under vigorous stirring to form a stable solution at room temperature. After ultrasonication for 30 min, a certain amount of Na_2S was dropped into the solution under vigorous stirring. Subsequently, this mixture was transferred to a 100 mL Teflon-lined autoclave and maintained at 180 °C for 24 h. Finally, the product that was obtained was filtered, washed with double-distilled water several times and dried at room temperature. After the precipitate cooled to room temperature naturally, a series of products (ZnS, $Zn_{0.5}Ag_{0.5}S$ and Ag_2S) were collected and utilized for further characterization.

Instruments and material characterization

Samples of the synthesized ZnS, $Zn_{0.5}Ag_{0.5}S$ and Ag_2S composites were characterized by various physicochemical techniques. The crystal structure of the samples was investigated using X-ray diffraction (XRD; Philips X'Pert Pro Advance X-ray diffractometer) with Cu Kα radiation over the range of 2θ = 10–80° with an accelerating voltage of 40 kV and an applied current of 40 mA. The size and shape of the prepared composite photocatalysts were observed by transmission electron microscopy (TEM, Tecnai G2) with an accelerating voltage of 200 kV. The morphology of the prepared photocatalysts was observed by scanning electron microscopy (SEM, Zeiss EVO MA-10, Germany) coupled with energy-dispersive X-ray spectroscopy (EDX) for determining the elemental composition. In order to study the absorption spectra of the samples (to calculate the E_g value), UV-visible diffuse-reflectance spectroscopy (UV-vis DRS, Shimadzu UV-3600 UV-vis-NIR spectrophotometer) was used, and $BaSO_4$ was used as a reflectance standard in the DRS experiments. The PL spectra of the photocatalysts were recorded using a Shimadzu RF-5301 PC spectrometer with an excitation wavelength of 335 nm. The specific surface areas of the samples were determined by Brunauer–Emmett–Teller (BET) measurements of nitrogen adsorption using an ASAP 2020 surface area and porosity analyzer. X-ray photoelectron spectroscopy (XPS) measurements were also performed with a monochromated Al Kα X-ray source ($h\nu$ = 1486.6 eV) at an energy of 15 kV per 150 W.

Photocatalytic reactor setup

Photocatalytic degradation experiments were performed in a slurry batch reactor to avoid exposure to UV light. A cylindrical photochemical reactor that measured 30 cm × 3 cm (height × diameter) and was equipped with a water circulation arrangement was used in all the experiments. Irradiation was carried out using UV lamps (300 W Xe lamps) built into a lamp housing with polished anodized aluminum reflectors and placed 6.5 cm from the reactor. Cooling was provided using a continuous flow of water through the middle cylinder to prevent the system from generating excess heat. The test solution was kept in the outer cylindrical part of the reactor. The lamps predominantly emitted UV radiation with a wavelength of 254 nm. The reactor setup was covered with aluminum foil followed by a black cloth to prevent leakage of UV light.

Pesticide degradation tests

The photocatalytic activities of the synthesized $Zn_xAg_{1-x}S$ materials were assessed by the photocatalytic degradation of MLT, MCP and CPS in an aqueous solution. Prior to the photocatalytic experiments, the adsorption of MLT, MCP and CPS on the ZnS, $Zn_{0.5}Ag_{0.5}S$ and Ag_2S composites used as the photocatalysts was carried out by mixing 100 mL of an aqueous solution of MLT, MCP or CPS, respectively, with a fixed weight of the respective photocatalyst (30 mg). Before irradiation with light, a suspension containing the organophosphorus pesticide and photocatalyst particles was sonicated for 10 min and vigorously stirred for 30 min in the dark to allow dispersion of the photocatalyst particles in the suspension and the attainment of sorption equilibrium, respectively. Then, the mixture was placed in a 100 mL quartz cell 30 cm from the UV light source in the photocatalytic reactor. During irradiation, 2.0 mL of the solution was sampled at regular intervals (10 min), and the concentrations of MLT, MCP and CPS were determined by measuring the absorbance at 265 nm, 210 nm and 226 nm, respectively, using a UV-visible absorption spectrometer. At given time intervals, aliquots of 2 mL were extracted and filtered by a membrane filter (pore size = 0.47 μm, diameter = 15 mm) for the removal of photocatalyst particles. From the degradation experiments, the percentage degradation of MLT, MCP and CPS using the $Zn_xAg_{1-x}S$ samples was determined by the following equation:

$$D(\%) = \frac{C_0 - C_t}{C_0} \times 100 \quad (1)$$

where D is the degradation efficiency and C_0 and C_t are the initial concentration and final concentration at time t of the MLT, MCP and CPS solutions, respectively.

Reactive oxidant species detection test

The generation of various active species was detected during the process of photoreaction. The major active species, namely, hydroxyl radicals ($^{\bullet}OH$), holes (h^+), and superoxide radicals ($^{\bullet}O_2^-$), were investigated by the addition of several scavengers, namely, *tert*-butyl alcohol (*t*-BuOH, 5 mmol L^{-1}), ammonium oxalate (AO, 1 mmol L^{-1}) and *p*-benzoquinone (*p*-BQ, 1 mmol L^{-1}), to the solutions of MLT, MCP and CPS, respectively, before irradiation with light using the $Zn_xAg_{1-x}S$ composites. The reusability of the catalysts was assessed by retrieving the catalysts after the degradation process followed by washing and drying in air at 110 °C. Then, the catalyst was reused for the degradation of MLT, MCP, and CPS under similar experimental conditions.

Results and discussion

Characterization of ternary semiconductor $Zn_xAg_{1-x}S$ photocatalysts

The phase composition and the crystal structure of the as-prepared samples were characterized by powder XRD. Fig. 1(a) shows the XRD patterns of the ternary $Zn_xAg_{1-x}S$ samples with different molar ratios. In the XRD pattern of pure ZnS, three prominent peaks corresponding to (111), (220), and (311) reflection planes were observed at 2θ values of 29.04°, 48.06°, and 57.11°, respectively, and can be indexed to the zinc blende structure (JCPDS card no: 05-0566). The broadening of the diffraction peaks might be due to the size effect, and therefore the crystallite size is in the nanoscale region. The powder XRD patterns of the $Zn_xAg_{1-x}S$ nanocomposites indicate a gradual phase change from cubic $Zn_xAg_{1-x}S$ (x = 1.0) (indexed to (111), (220), and (311) planes) to monoclinic $Zn_xAg_{1-x}S$ (x = 0.5), with peaks indexed to (101), (110), (120), (112), (031), (103), (123) and (−213) planes and, with an increase in the Ag content, at 45.15° (200) and 64.21° (220). This phenomenon signifies the incorporation of Ag atoms into the lattice of ZnS, which influenced the positions of Zn atoms and subsequently changed the lattice structure of ZnS in the process of formation of solid solutions of $Zn_xAg_{1-x}S$ under the synthetic conditions. The results show that the crystal phases of ZnS changed after it combined with the Ag content, which further suggests that this may be beneficial for the photocatalytic properties of the composite photocatalysts. Furthermore, a careful examination of the powder XRD patterns revealed a shift in the 2θ values of the peaks with an increase in the Ag content. The observed shift in the positions of the peaks of ZnS (2θ) is attributed to the incorporation of larger Ag^+ ions (ionic radius = 1.14 Å) in the positions of Zn^{2+} ions (ionic radius = 0.74 Å) in the lattice of ZnS, which may indicate that the $Zn_{0.5}Ag_{0.5}S$ composite photocatalyst was in the form of a composite instead of a simple mixture. The estimated crystallite size of the $Zn_xAg_{1-x}S$ composites was 10–30 nm as determined by the Debye–Scherrer equation using the peak of highest intensity in the diffraction patterns.

The UV-vis DRS spectra of the samples were recorded using a UV-vis spectrophotometer to study the optical absorption properties of the prepared photocatalysts. The room-temperature solid-state UV-vis DRS spectra of the $Zn_{0.5}Ag_{0.5}S$ composite, ZnS and Ag_2S in the wavelength range of 200–800 nm are shown in Fig. 1(b). The spectra show a red shift in the absorption edge from 400 to 610 nm with an increase in the Ag

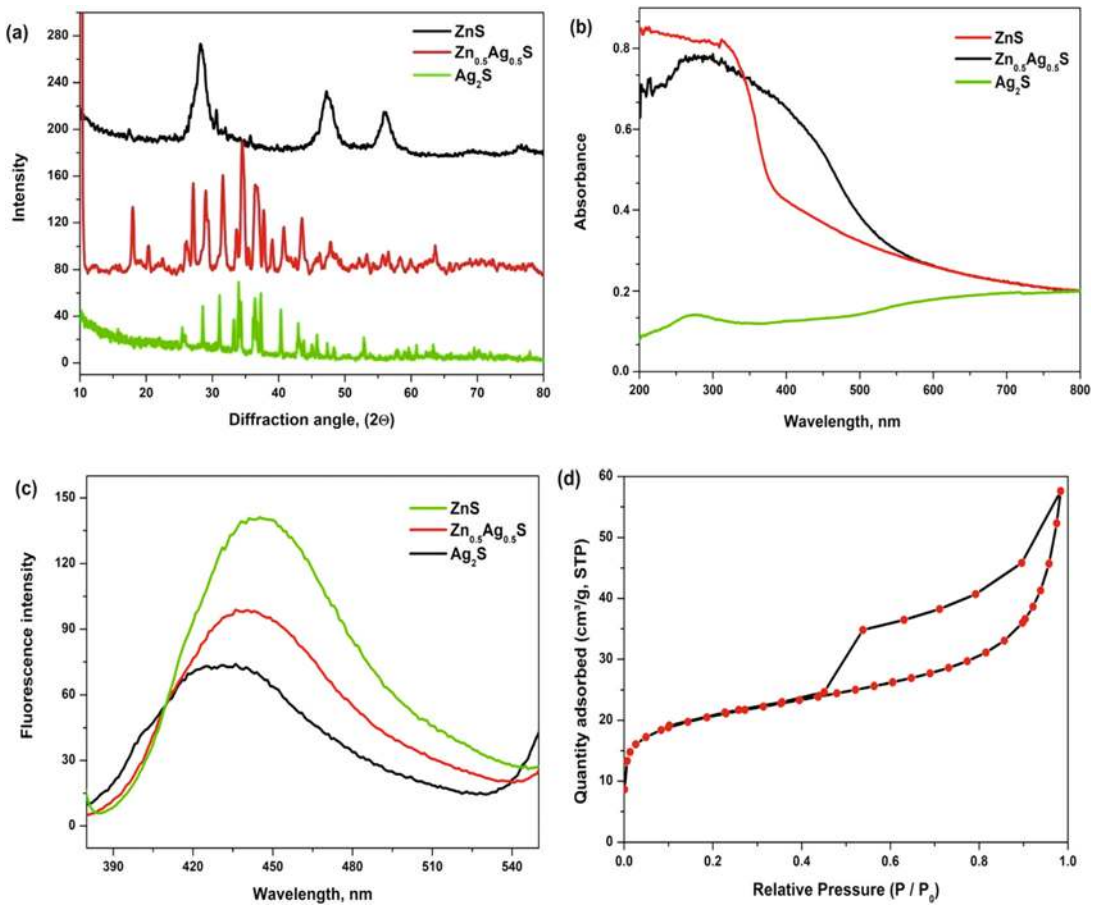

Fig. 1 (a) Powder XRD patterns, (b) UV-vis DRS and (c) PL spectra of the $Zn_xAg_{1-x}S$ (x = 0, 0.5 and 1.0) nanocomposites, and (d) N_2 adsorption/desorption isotherm of the $Zn_{0.5}Ag_{0.5}S$ nanocomposite.

content in the $Zn_xAg_{1-x}S$ composites, with the absorption edges of ZnS and Ag_2S at 360 and around 680 nm, respectively. The red shift in the absorption edge of the composites was due to the amount of Ag present, and the absorption edge was also situated between those of ZnS and Ag_2S. The presence of Ag can accelerate the separation of photogenerated charge carriers and thus improve the light absorption efficiency of ZnS. This phenomenon can be attributed to an intrinsic band gap transition rather than a transition from impurity levels, which suggests the formation of $Zn_{0.5}Ag_{0.5}S$ composites. Thus, the $Zn_xAg_{1-x}S$ nanocomposites exhibited sharp absorption band edges in the visible region. This implies that $Zn_{0.5}Ag_{0.5}S$ was not a simple mixture of ZnS and Ag_2S but comprised composites of $Zn_xAg_{1-x}S$ with various compositions (x = 0.5). The calculated band edges of the ZnS and Ag_2S samples were located at around 360 nm (3.44 eV) and 680 nm (1.82 eV), which correspond to UV and visible light absorption, respectively. Moreover, the calculated band gap of $Zn_{0.5}Ag_{0.5}S$ is 2.54 eV. This range of band gaps and the energy levels of the semiconductors play a crucial role in improving their photocatalytic properties.

PL spectroscopy is an important characterization technique for determining charge carrier trapping, charge migration and recombination of light-generated electron–hole pairs in a semiconductor.[42,43] Fig. 1(c) shows the PL spectra of the ZnS, $Zn_{0.5}Ag_{0.5}S$ and Ag_2S samples, which were excited at 350 nm and exhibited emission peaks at around 452, 447 and 438 nm, respectively, and the decrease in the emission intensity may be related to the recombination process and an enhancement in photocatalytic activity. The change in the position of the PL peak of the $Zn_{0.5}Ag_{0.5}S$ composite indicates that the Ag content in the ZnS lattice promoted the dissociation of light-induced electrons from holes with no significant alteration in the position of the PL band. In addition, this effect was further reinforced after decoration with ZnS and Ag_2S to form the $Zn_{0.5}Ag_{0.5}S$ composite, which implies that the interface between Zn^{2+} and Ag^{+} hinders the recombination of charge carriers and encourages their efficient separation, which leaves more to participate in the photodegradation of pesticides. This clearly indicates a significant decrease in emission intensity for $Zn_{0.5}Ag_{0.5}S$, which confirms that the recombination process was slow in comparison with that in the pure ZnS and Ag_2S samples. The PL results prove that the decrease in emission intensity promoted higher photocatalytic activity.

To determine the surface area of the as-prepared samples, N_2 adsorption/desorption measurements were performed for the $Zn_xAg_{1-x}S$ nanocomposites in the range of relative pressures of 0.1–1.0. Fig. 1(d) shows the N_2 adsorption/desorption isotherm of the $Zn_{0.5}Ag_{0.5}S$ composite. The isotherm was identified as type IV, which is characteristic of mesoporous materials.[44] The pore size distribution calculated from the isotherm indicates the presence of a number of pores with sizes of less than 10 nm in the sample. The estimated BET surface areas of the samples of ZnS, $Zn_{0.5}Ag_{0.5}S$, and Ag_2S are 16.37, 68.02, and 23.52 $m^2\ g^{-1}$, respectively. The large BET surface area of the sample of the $Zn_{0.5}Ag_{0.5}S$ composite strongly supports the assumption that the nanoparticles have a nanoporous structure. The large surface area of the $Zn_{0.5}Ag_{0.5}S$ composite enables the efficient adsorption and transport of charge carriers, which leads to an enhancement in the photocatalytic performance.

Analysis of the nanocomposites using SEM supplemented by EDX was carried out for the $Zn_xAg_{1-x}S$ samples to establish their morphology, grain size, and shape and to confirm their chemical composition. Fig. 2(a–c) shows scanning electron micrographs of samples of the ZnS, $Zn_{0.5}Ag_{0.5}S$, and Ag_2S composites. Typical scanning electron microscopy (SEM) images of the samples are presented in Fig. 2, in which the morphology of spherical nanoparticles is also clearly visible. The surface of every particle is rough, and there are many smaller particles. At a low magnification, the dispersion of nanoparticles is not clearly identified, as they are agglomerated. Furthermore, high-magnification images show the presence of nanocrystals on the surface of the microspheres (Fig. 2(a–c)). Thus, it is clear from the high-resolution SEM images that slight agglomeration of particles occurred. For elemental analysis, EDX data (Fig. 2(d–f)) are also reported with the SEM images and confirm the presence of Zn, Ag, S, C, and O in the samples of the $Zn_xAg_{1-x}S$ composites.

From the SEM images it is seen that agglomeration of particles occurred, and hence the actual size of the crystallites is not clear. Hence, HR-TEM analyses were carried out for the precise determination of the crystallite size. Fig. 3(a–e) shows low-resolution and high-resolution TEM images of ZnS, $Zn_{0.5}Ag_{0.5}S$ and Ag_2S samples, which show the presence of nanocrystals with sizes of 10–50 nm and spherical shapes but no uniform size. An observation of the HR-TEM images reveals the lattice pattern in the nanocrystals, which indicates the polycrystalline nature of the material. This clearly illustrates the altered size and morphology of the catalyst powder and enhanced photocatalytic activity, which is due to the decrease in the particle size and increase in the surface area of the catalyst. The estimated values of the crystallite size are consistent with the crystallite sizes calculated from the XRD pattern. The TEM observations clearly confirm that Ag particles were well dispersed on the ZnS surface. By combining the structural (XRD) and morphological (TEM) analyses mentioned above, it could be deduced that the synthesized $Zn_xAg_{1-x}S$ composite system is formed from mixed phases, but the dominant phase is a zinc blende phase. The HRTEM images of the $Zn_{0.5}Ag_{0.5}S$ nanocomposite (Fig. 3(d and e)) show a clear interface between ZnS and Ag. Therefore, the present ternary photocatalytic system exhibits a close interconnection between ZnS and Ag nanoparticles at a single point, which is necessary for charge transfer during photoreactions. The SAED pattern (Fig. 3(f)) exhibits well-defined electron diffraction spots, which confirm the crystalline nature of the cubic phase of the ZnS nanocrystals. Moreover, $Zn_{0.5}Ag_{0.5}S$ displays circular rings corresponding to diffraction planes of ZnS. From these patterns, it is clear that the crystallinity of the nanoparticles increased with the incorporation of Ag ions, as a dot pattern started to

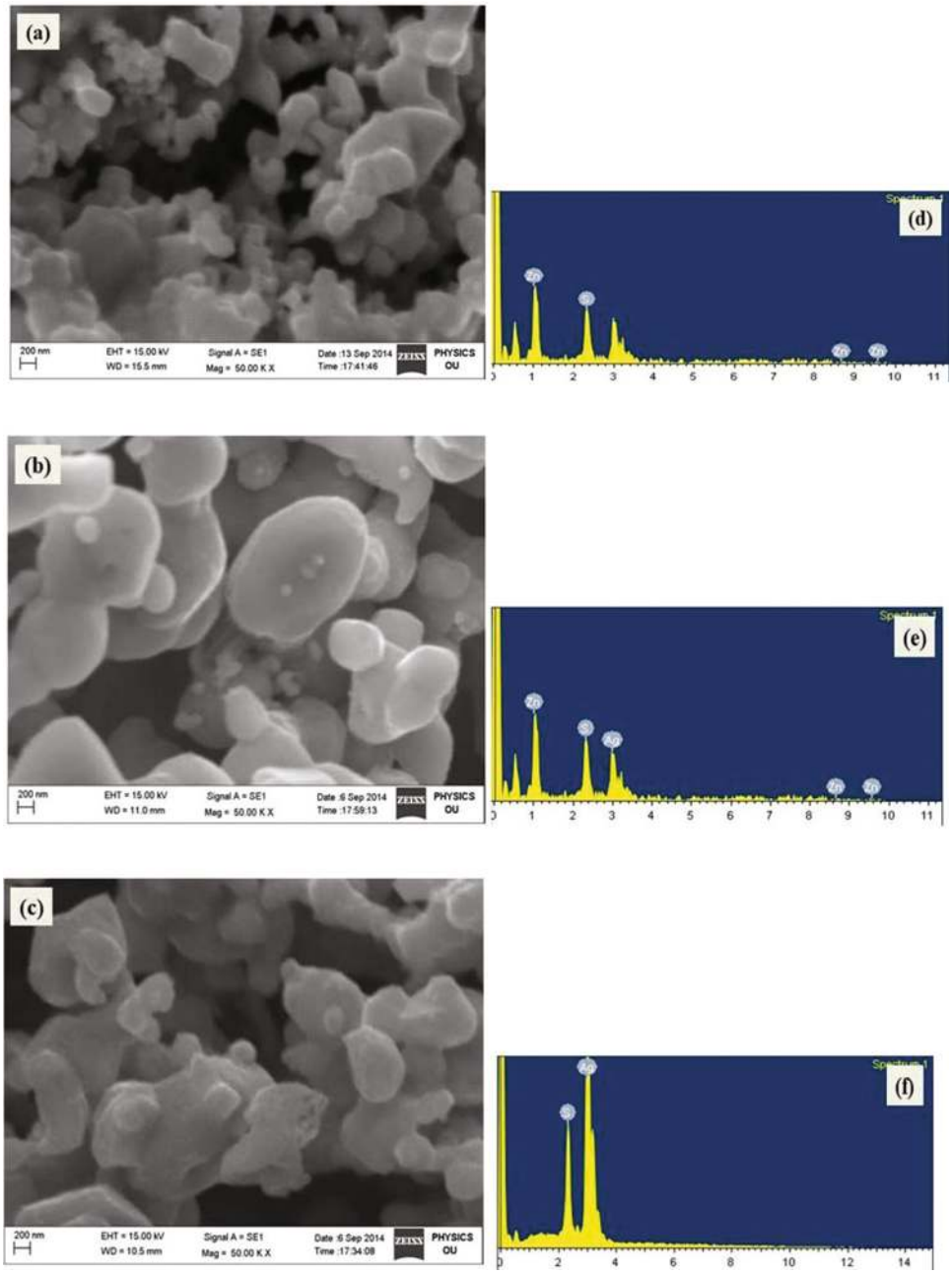

Fig. 2 (a–c) SEM images and (d–f) the corresponding EDX maps of the $Zn_xAg_{1-x}S$ (x = 0, 0.5 and 1.0) nanocomposites, respectively.

appear; this confirms the formation and polycrystalline nature of the product.

The surface chemical composition and chemical states of the $Zn_xAg_{1-x}S$ composite were examined by XPS and are shown in Fig. 4. The XPS survey spectrum of the synthesized photocatalyst revealed the presence of Zn, C, O, and Ag with no impurities (Fig. 4(a)). In order to further investigate the surface composition of the $Zn_{0.5}Ag_{0.5}S$ composite, the XPS survey spectrum and the corresponding O 1s, S 2p, Zn 2p, and C 1s spectra were studied. In the survey spectrum, peaks resulting from S 2p, Zn 2p, Ag 3d, C 1s, and O 1s were conspicuously observed at the respective standard values of binding energies, which confirmed the presence of these elements in the synthesized nanocomposites. The peaks at 1044.8 and 1021.9 eV were attributed to spin–orbit splitting of the Zn 2p orbital and were assigned to Zn $2p_{1/2}$ and Zn $2p_{3/2}$, respectively (Fig. 4(b)).[45] Fig. 4(c) shows the narrow-scan XPS spectrum of the core-level binding energy of Ag^+ in the energy range of 364–378 eV. It shows that the high-resolution XPS spectrum of Ag 3d could be decomposed into Ag $3d_{5/2}$ and Ag$3d_{3/2}$ peaks at binding energies of 367.82 eV and 375.71 eV, respectively. The difference between the binding energy of Ag $3d_{5/2}$ (367.82 eV) and Ag $3d_{3/2}$ (375.71 eV) is 7.89 eV, which is characteristic of metallic Ag in the matrix of an Ag_2S product.[46] The S 2p peak

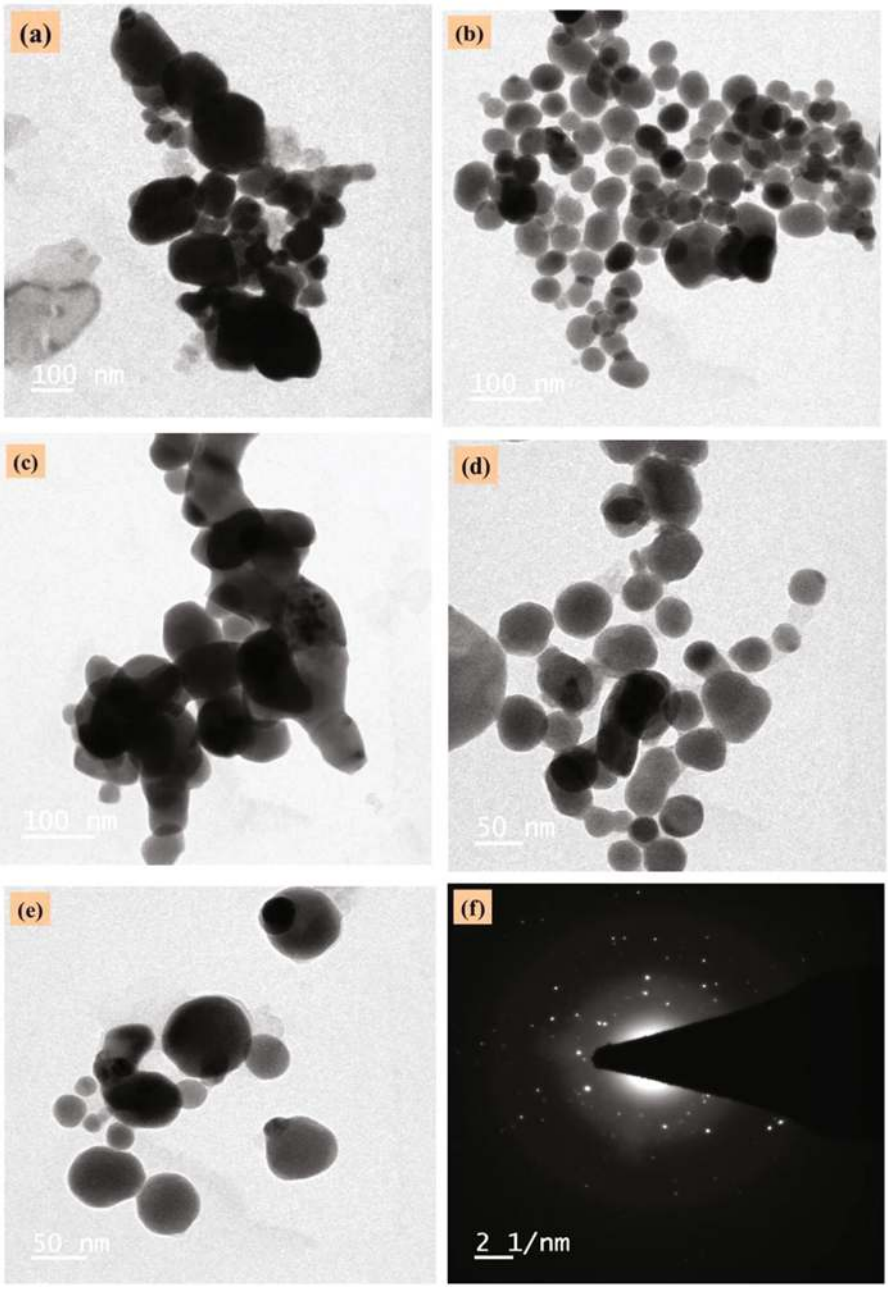

Fig. 3 (a–c) Low-resolution and (d–e) high-resolution TEM images of the ZnS, $Zn_{0.5}Ag_{0.5}S$ and Ag_2S composites and (f) SAED pattern of the $Zn_{0.5}Ag_{0.5}S$ composite.

(Fig. 4(d)) and Zn 2p peaks can be observed at 163.31 eV and 1021.9/1044.8 eV, which suggests that S and Zn elements exist mainly in the form of S^{2-} and Zn^{2+}, respectively, on the surface of the samples.[47] In summary, the XPS spectra confirm that the positions of the peaks due to Zn, Ag, and S correspond to a $Zn_{0.5}Ag_{0.5}S$ nanocomposite.

Photocatalytic degradation of organophosphorus pesticides

As determined from the optical measurements, all the synthesized photocatalysts were expected to exhibit photocatalytic activity under UV light. Therefore, photocatalytic degradation studies were conducted using the $Zn_xAg_{1-x}S$ composites for the degradation of organophosphorus pesticides, namely, MLT, MCP, and CPS, as model pollutants under UV light irradiation. Pretreatment of the synthesized photocatalysts with solutions of MLT, MCP, and CPS in the dark gave an adsorption rate of <11% in all cases under UV light irradiation for 1 h. The effect of photolysis was confirmed before the photodegradation study by irradiating the solutions with a light source in the absence of a catalyst. As shown in Fig. S1(a–c),† photolysis had no pronounced effect on the degradation of MLT, MCP, and CPS under UV light irradiation, whereas the

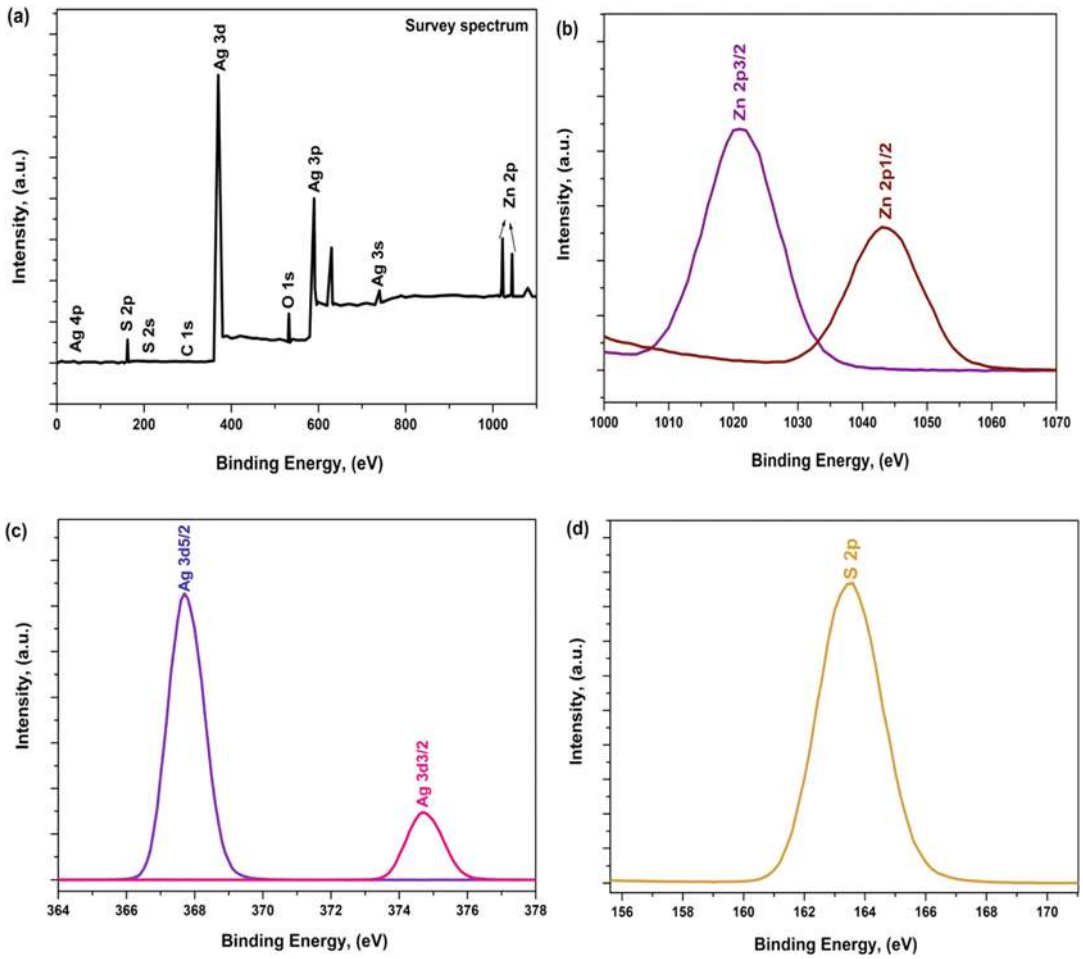

Fig. 4 High-resolution X-ray photoelectron spectra of the $Zn_{0.5}Ag_{0.5}S$ nanocomposite: (a) survey, (b) Zn 2p, (c) Ag 3d, and (d) S 2p spectra of a representative sample.

presence of pure ZnS resulted in degradation rates of 82.38% (MLT), 79.51% (MCP) and 80.27% (CPS), and pure Ag_2S resulted in degradation rates of 80.12% (MLT), 76.51% (MCP) and 78.72% (CPS) after 60 min under similar conditions. For comparison, the activities of samples of pure ZnS and Ag_2S were also tested under the same conditions (Fig. 5). It can be seen from Fig. 5 that in comparison with pure ZnS and Ag_2S the $Zn_{0.5}Ag_{0.5}S$ composite material displayed higher photocatalytic performance because of the presence of Ag ions incorporated into the ZnS lattice for the transfer of charge carriers, large surface area, and smaller particle size. The enhancement in the photodegradation of MLT, MCP, and CPS after treatment with the $Zn_{0.5}Ag_{0.5}S$ ternary photocatalyst under UV light irradiation is clearly observed in Fig. S2(a–c).† The remarkable enhancement in the UV-light-driven photocatalytic activity of the $Zn_{0.5}Ag_{0.5}S$ composite was mainly due to the enhanced charge separation and UV light harvesting properties of the Ag nanoparticles.[48,49] Moreover, the Ag nanoparticles anchored on the surface of $Zn_{0.5}Ag_{0.5}S$ behave as an electron sink, which could significantly increase the separation of photogenerated electron–hole pairs and inhibit their recombination.[50] The

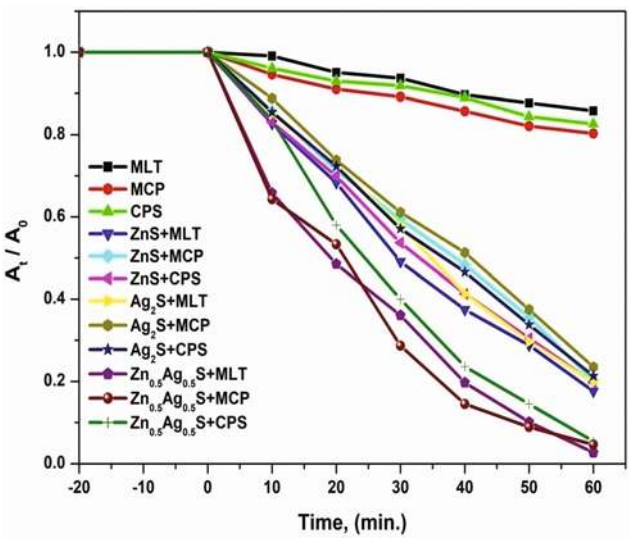

Fig. 5 The photocatalytic degradation of the organophosphorus pesticides MLT, MCP and CPS was monitored *via* the UV-visible absorption spectra of a reaction mixture containing the $Zn_xAg_{1-x}S$ composite photocatalysts.

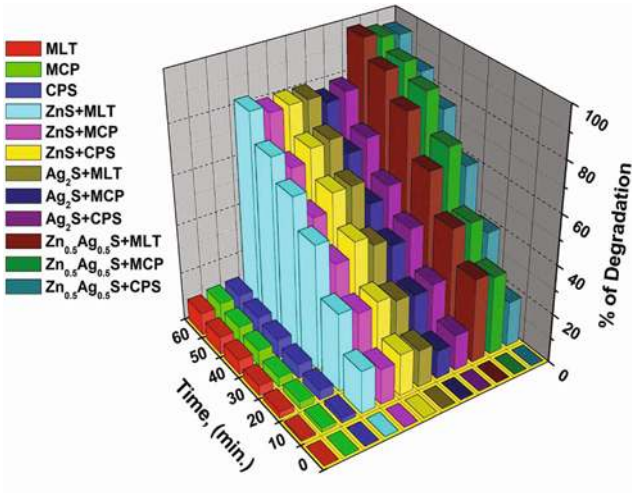

Fig. 6 3D bar diagram of the photocatalytic degradation of MLT, MCP and CPS in the absence and presence of the $Zn_xAg_{1-x}S$ composite photocatalysts.

enhanced photocatalytic performance of the $Zn_{0.5}Ag_{0.5}S$ composite is due to the presence of Ag^0 formed by the photoreduction of Ag^+ under light irradiation. The order of the photocatalytic activities in the degradation of MLT, MCP, and CPS under similar conditions was Ag_2S < ZnS < $Zn_{0.5}Ag_{0.5}S$, which further confirms that the Ag nanoparticle loading plays a crucial role in the photocatalytic properties.[49] It is clearly seen from Fig. 6 that the rate of photocatalytic degradation for the $Zn_{0.5}Ag_{0.5}S$ composite photocatalyst was much higher in comparison with those for pure ZnS and Ag_2S under similar conditions.

On the basis of the detailed characterization and previous reports,[51–54] a probable mechanism of the enhanced photocatalytic performance of the $Zn_{0.5}Ag_{0.5}S$ composite under UV light irradiation was proposed for the degradation of MLT, MCP, and CPS (Scheme 1). In this study, the recombination of photogenerated charges produced by the absorption of UV light by oxygen vacancies resulted in a lower band gap, which was extended by the transfer of electrons from the conduction band

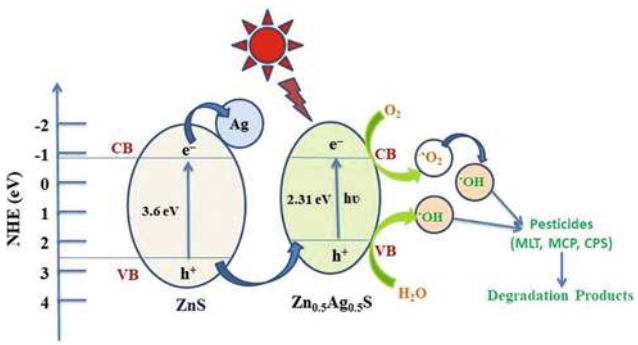

Scheme 1 Schematic representation of photocatalytic degradation of organophosphorus pesticides using the $Zn_{0.5}Ag_{0.5}S$ composite photocatalysts.

of ZnS to the highest occupied molecular orbital of Ag. On the other hand, Ag can also act as a sensitizer to absorb UV light and transfer electrons from the surface of Ag to the conduction band of ZnS. In addition to these excitations, in the case of the present ternary photocatalytic system, Ag nanoparticles act as a photocenter to generate electron–hole pairs by the absorption of UV light *via* the SPR effect. A number of excitations are possible in the present case because the Ag nanoparticles are strongly interconnected with the $Zn_{0.5}Ag_{0.5}S$ composite. The SPR effect produced by UV light irradiation leads to the transfer of electrons from the equilibrium Fermi level to the conduction band of ZnS, which leaves holes behind on the Ag surface. These electrons injected into the CB of ZnS can either react with dissolved oxygen to produce superoxide radical anions ($^{\bullet}O_2^-$), which can subsequently react with H_2O to give hydroxyl radicals ($^{\bullet}OH$) in a consecutive reaction pathway. In another case, the photogenerated electrons are transferred directly to the Ag surface from the CB of ZnS and react with dissolved oxygen to form oxidizing radicals. The holes formed by the absorption of UV light by ZnS and Ag can react with hydroxyl groups to generate hydroxyl radicals. The free radicals produced by the overall process react further with organic pollutants (in the present case, the pesticides MLT, MCP, and CPS) to oxidize them to CO_2, H_2O, and other products.

In order to determine the degradation products of the photocatalytic activity of the ZnS, $Zn_{0.5}Ag_{0.5}S$, and Ag_2S photocatalysts, a series of experiments were carried out with MLT, MCP, and CPS in an aqueous suspension with UV light with a wavelength of 254 nm. As the irradiation time increased, MLT, MCP, and CPS degraded into small fragments, and consequently complete mineralization was achieved in about 1 h. To complete the degradation of the pesticide compounds using the $Zn_{0.5}Ag_{0.5}S$ composite photocatalyst required a shorter irradiation time than with pure ZnS and Ag_2S. This was due to the suppression of electron–hole recombination and the generation of more $^{\bullet}OH$ radicals. The $^{\bullet}OH$ radicals are sufficiently reactive to break different (C–C, C=C, and C=O) bonds in MLT, MCP, and CPS molecules adsorbed on the surface of the $Zn_xAg_{1-x}S$ composites, which will finally lead to the formation of CO_2 and inorganic ions. Furthermore, the continuous degradation of MLT, MCP, and CPS leads to the formation of intermediates such as aldehydes, alcohols, nitrates and phosphoric acid. The alcohols and aldehydes can easily be hydrolyzed in water, whereas the phosphoric acid and nitrates are transformed into harmless inorganic ions such as phosphate (PO_4^{3-}) and nitrate (NO_3^-). Finally, MLT, MCP and CPS and their intermediates are converted into CO_2, H_2O and harmless inorganic ions.

To further investigate the active species in the process of the photocatalytic degradation of MLT, MCP and CPS by the $Zn_xAg_{1-x}S$ nanocomposites under UV light irradiation, it is well known that hydroxyl radicals ($^{\bullet}OH$), valence band holes (h^+) and superoxide radicals ($^{\bullet}O_2^-$) have been deemed to be the main reactive species in the process of the photocatalytic degradation of organic pollutants. Radical scavengers, namely, *t*-BuOH, *p*-BQ, and AO, were employed for the investigation of

$^{\bullet}OH$ and $^{\bullet}O_2^-$ radicals and valence band holes (h^+) generated during the $Zn_{0.5}Ag_{0.5}S$-assisted photocatalytic process. As shown in Fig. 7(a–c), the addition of these quenchers inhibited the photocatalytic activity of $Zn_{0.5}Ag_{0.5}S$ under UV light for the degradation of MLT, MCP, and CPS. The degradation efficiency for MLT, MCP, and CPS decreased greatly on the addition of *p*-BQ in comparison with the addition of *t*-BuOH and AO. It is indicated that $^{\bullet}O_2^-$ radicals played a critical role in the photocatalytic activity of the $Zn_{0.5}Ag_{0.5}S$ composite in comparison with h^+ and $^{\bullet}OH$ radicals under UV light irradiation. It is concluded that $Zn_{0.5}Ag_{0.5}S$ can suppress the recombination of induced electron–hole pairs under visible light irradiation. Similarly, we investigated the scavenging effect of ZnS and Ag_2S samples in the degradation of MLT, MCP, and CPS, and the results are shown in Fig. S3(a–c) and S4(a–c),† respectively.

The stability of a photocatalyst sample is important for practical applications. The ternary semiconductor $Zn_xAg_{1-x}S$ photocatalyst displayed the best charge separation ability and highest photocatalytic performance among all the catalysts that were prepared (Fig. 8(a–c), Fig. S5(a–c) and S6(a–c)†).

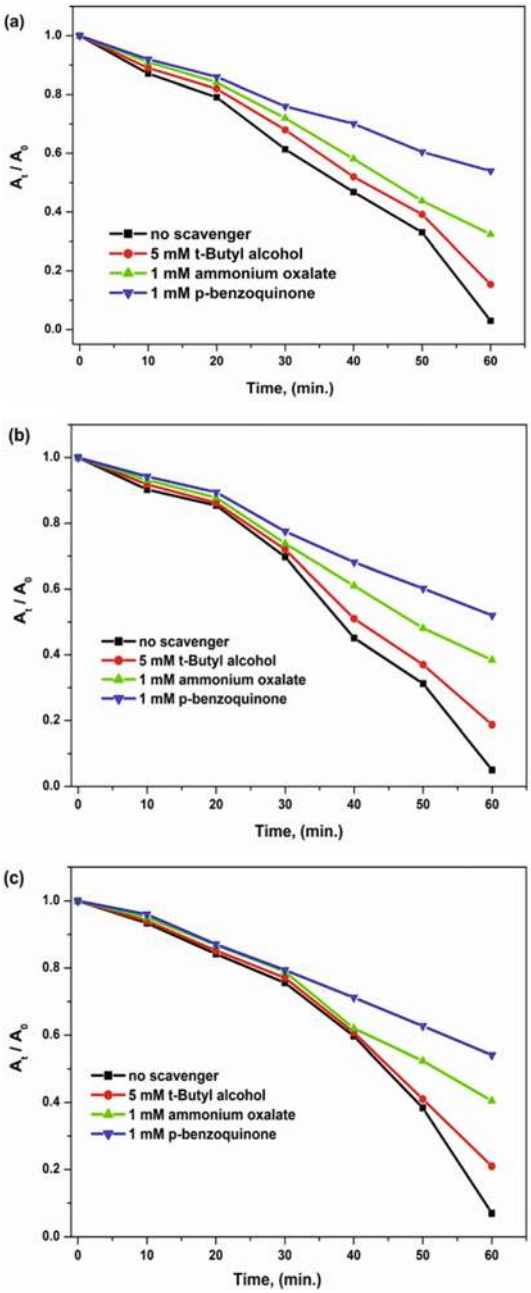

Fig. 7 Effects of the addition of different scavengers on the photocatalytic degradation of (a) MLT, (b) MCP and (c) CPS by the $Zn_{0.5}Ag_{0.5}S$ composite photocatalyst.

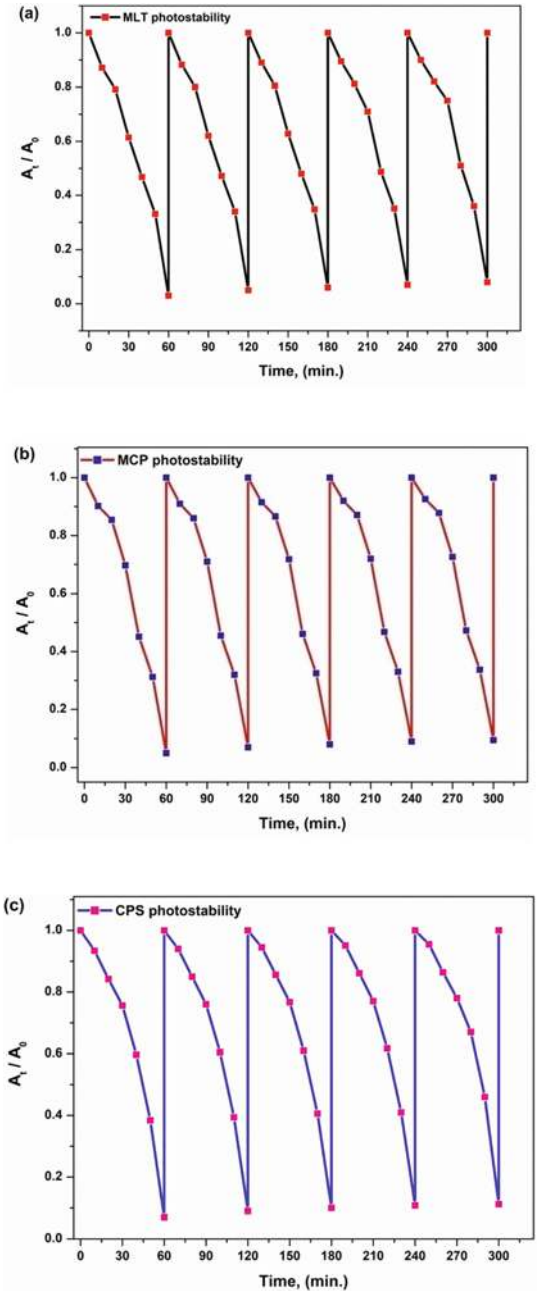

Fig. 8 Cycling runs in the photocatalytic degradation of (a) MLT, (b) MCP and (c) CPS in the presence of the synthesized $Zn_{0.5}Ag_{0.5}S$ composite photocatalyst under UV light irradiation.

Therefore, the photocatalytic stability of the $Zn_{0.5}Ag_{0.5}S$ composite was examined by performing recycling experiments for the photodegradation of MLT, MCP, and CPS under UV light irradiation. As shown in Fig. 8, the ternary semiconductor $Zn_{0.5}Ag_{0.5}S$ photocatalyst exhibited superior photostability, which remained roughly unchanged after five successive cycles. The used photocatalysts after each run were collected, centrifuged, washed with distilled water, dried at 100 °C and then reused in a new run. As illustrated, at the end of the fifth run the degradation efficiency declined from 96.41% to 94.27% (MLT), from 92.51% to 90.64% (MCP) and from 91.38% to 89.61% (CPS) using the $Zn_{0.5}Ag_{0.5}S$ composite photocatalyst. The slight decrease in photocatalytic activity may be due to the inevitable loss of the catalyst during the washing, centrifugation, sedimentation and transfer processes,[55] and no changes were observed in the structure and morphology of the $Zn_{0.5}Ag_{0.5}S$ catalyst. The enhanced photostability in support of the photocatalytic activity favors the practical application of the ternary $Zn_{0.5}Ag_{0.5}S$ composite photocatalysts.

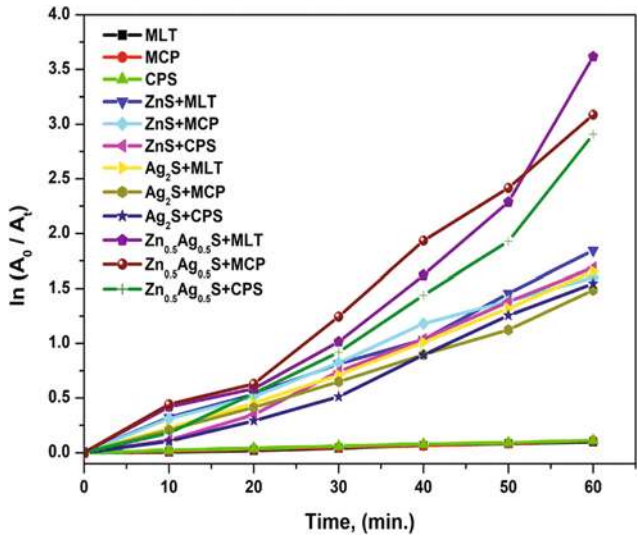

Fig. 9 Kinetic plots of the photocatalytic degradation of MLT, MCP, and CPS in the absence and presence of the synthesized $Zn_xAg_{1-x}S$ composite photocatalysts.

To further study the reaction kinetics, the photodegradation of MLT, MCP, and CPS using samples of the $Zn_xAg_{1-x}S$ composites was fitted to a pseudo-first-order kinetic equation,[56] and the results that were obtained are shown in Fig. 9. This clearly indicates that the photocatalytic activity of $Zn_{0.5}Ag_{0.5}S$ is higher than that of the ZnS and Ag_2S samples under UV light irradiation. It can be deduced from these results that $Zn_{0.5}Ag_{0.5}S$ possessed the best photocatalytic activity under UV light irradiation, which may indicate that the transfer of photogenerated holes and electrons and the adsorption capacity reached an optimum in this composite photocatalyst. The apparent rate constant (k) for the degradation of MLT, MCP, and CPS by the $Zn_{0.5}Ag_{0.5}S$ composite photocatalyst, which was determined by linear estimation using pseudo-first-order reaction kinetics, was calculated to be 0.01281, 0.01254 and 0.01211 min^{-1}, which was an average of 1.38 and 1.57 times higher than those for pure Ag_2S and ZnS, respectively. The maximum photocatalytic performance of the $Zn_{0.5}Ag_{0.5}S$ photocatalyst for the degradation of MLT, MCP, and CPS was higher than that of pure Ag_2S and ZnS, which was basically related to the SPR effect of Ag ions in the ZnS lattice. The degradation efficiencies, apparent reaction rate constants (k) and $t_{1/2}$ values of the ZnS, $Zn_{0.5}Ag_{0.5}S$ and Ag_2S samples are summarized in Table 1.

Table 1 Comparison of photocatalytic activity of various catalysts for degrading the organophosphorus pesticides MLT, MCP, and CPS

Catalyst	Organophosphorus pesticide	% of degradation	Rate constant, (min^{-1})	Half-life (min)	R^2
No catalyst	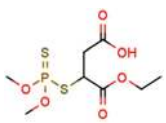	8.94	0.00101	686.14	0.98
ZnS		82.38	0.00961	72.11	0.99
$Zn_{0.5}Ag_{0.5}S$		97.31	0.01281	54.09	0.97
Ag_2S		80.12	0.00816	84.92	0.99
	MLT				
No catalyst	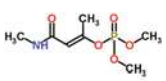	10.11	0.00107	647.66	0.99
ZnS		79.51	0.00914	75.82	0.99
$Zn_{0.5}Ag_{0.5}S$		95.44	0.01254	55.26	0.98
Ag_2S		76.51	0.00751	92.27	0.99
	MCP				
No catalyst	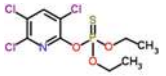	10.47	0.00109	635.78	0.99
ZnS		80.27	0.00932	74.35	0.99
$Zn_{0.5}Ag_{0.5}S$		94.54	0.01211	57.22	0.98
Ag_2S		78.72	0.00784	88.39	0.97
	CPS				

Conclusions

In summary, ternary semiconductor $Zn_xAg_{1-x}S$ composites were prepared for the UV-light-driven photodegradation of organophosphorus pesticides (MLT, MCP, and CPS) *via* a hydrothermal route without using any surfactant. The samples that were prepared were unambiguously characterized by XRD, XPS, UV-vis DRS, PL, BET measurements, SEM-EDX, and TEM. Among all the prepared samples, $Zn_{0.5}Ag_{0.5}S$ possessed pre-eminent photocatalytic activity in the degradation of MLT, MCP, and CPS under UV light. The degradation efficiency reached 95% after irradiation for 1 h, which was higher than that of the pure ZnS and Ag_2S samples. The higher photocatalytic degradation rate of MLT, MCP, and CPS was achieved using the $Zn_{0.5}Ag_{0.5}S$ composite because the synergetic effect of the Ag content played an important role in the transfer of charge carriers during the photocatalytic degradation process, which effectively prolonged the lifetime of photoinduced electrons generated by Ag and ZnS upon the absorption of UV light. Active oxygen species ($^{\bullet}O_2^-$ and $^{\bullet}OH$) and h^+ played an important role in the degradation process. The enhanced photocatalytic activity and photostability suggest that the ternary $Zn_xAg_{1-x}S$ photocatalyst has potential applications in water treatment.

Conflicts of interest

There are no conflicts to declare.

Acknowledgements

The authors would like to acknowledge the Head, Department of Chemistry, Osmania University for providing the necessary facilities. The authors would like to thank DST–FIST, New Delhi, India for providing necessary analytical facilities in the department.

References

1 M. N. Chong, B. Jin, C. W. Chow and C. Saint, Recent developments in photocatalytic water treatment technology: a review, *Water Res.*, 2010, **44**, 2997–3027.
2 N. Savage and M. S. Diallo, Nanomaterials and water purification: opportunities and challenges, *J. Nanopart. Res.*, 2005, **7**, 331–342.
3 D. Ayodhya and G. Veerabhadram, Green synthesis characterization, photocatalytic, fluorescence and antimicrobial activities of Cochlospermum gossypium capped Ag_2S nanoparticles, *J. Photochem. Photobiol., B*, 2016, **157**, 57–69.
4 A. Fakhri and P. A. Nejad, Antimicrobial, antioxidant and cytotoxic effect of Molybdenum trioxide nanoparticles and application of this for degradation of ketamine under different light illumination, *J. Photochem. Photobiol., B*, 2016, **159**, 211–217.
5 D. Ayodhya and G. Veerabhadram, Preparation, characterization, photocatalytic, sensing and antimicrobial studies of Calotropis gigantea leaf extract capped CuS NPs by a green approach, *J. Inorg. Organomet. Polym.*, 2017, **27**, 215–230.
6 L. A. Ioannou, E. Hapeshi, M. I. Vasquez, D. Mantzavinos and D. Fatta-Kassinos, Solar/TiO_2 photocatalytic decomposition of β-blockers atenolol and propranolol in water and wastewater, *Sol. Energy*, 2011, **85**, 1915–1926.
7 N. Ajoudanian and A. Nezamzadeh-Ejhieh, Enhanced photocatalytic activity of nickel oxide supported on clinoptilolite nanoparticles for the photodegradation of aqueous cephalexin, *Mater. Sci. Semicond. Process.*, 2015, **36**, 162–169.
8 D. Ayodhya and G. Veerabhadram, A review on recent advances in photodegradation of dyes using doped and heterojunction based semiconductor metal sulfide nanostructures for environmental protection, *Mater. Today Energy*, 2018, **9**, 83–113.
9 H. Park, H. I. Kim, G. H. Moon and W. Choi, Photoinduced charge transfer processes in solar photocatalysis based on modified TiO_2, *Energy Environ. Sci.*, 2016, **9**, 411–433.
10 B. Jin, X. Li, X. Zhou, X. Xu, H. Jian, M. Li, K. Guo, J. Guan and S. Yan, Fabrication and characterization of nanocomposite film made from a jackfruit filum polysaccharide incorporating TiO_2 nanoparticles by photocatalysis, *RSC Adv.*, 2017, **7**, 16931–16937.
11 N. K. R. Eswar, P. C. Ramamurthy and G. Madras, High photoconductive combustion synthesized TiO_2 derived nanobelts for photocatalytic water purification under solar irradiation, *New J. Chem.*, 2015, **39**, 6040–6051.
12 L. Ye, X. Jin, Y. Leng, Y. Su, H. Xie and C. Liu, Synthesis of black ultrathin BiOCl nanosheets for efficient photocatalytic H_2 production under visible light irradiation, *J. Power Sources*, 2015, **293**, 409–415.
13 K. V. A. Kumar, S. R. Amanchi, B. Sreedhar, P. Ghosal and C. Subrahmanyam, Phenol and Cr(VI) degradation with Mn ion doped ZnO under visible light photocatalysis, *RSC Adv.*, 2017, **7**, 43030–43039.
14 L. Rimoldi, D. Meroni, E. Falletta, V. Pifferi, L. Falciola, G. Cappelletti and S. Ardizzone, Emerging pollutant mixture mineralization by TiO_2 photocatalysts. The role of the water medium, *Photochem. Photobiol. Sci.*, 2017, **16**, 60–66.
15 N. K. R. Eswar, P. C. Ramamurthy and G. Madras, Enhanced sunlight photocatalytic activity of Ag_3PO_4 decorated novel combustion synthesis derived TiO_2 nanobelts for dye and bacterial degradation, *Photochem. Photobiol. Sci.*, 2015, **14**, 1227–1237.
16 D. Ayodhya and G. Veerabhadram, Hydrothermally generated and highly efficient sunlight responsive SiO_2 and TiO_2 capped Ag_2S nanocomposites for photocatalytic degradation of organic dyes, *J. Environ. Chem. Eng.*, 2018, **6**, 311–324.
17 C. M. Chang, K. L. Orchard, B. C. Martindale and E. Reisner, Ligand removal from CdS quantum dots for enhanced photocatalytic H_2 generation in pH neutral water, *J. Mater. Chem.*, 2016, **4**, 2856–2862.

18 D. Ayodhya, M. Venkatesham, A. S. Kumari, G. B. Reddy, D. Ramakrishna and G. Veerabhadram, Photocatalytic degradation of dye pollutants under solar, visible and UV lights using green synthesised CuS nanoparticles, *J. Exp. Nanosci.*, 2016, **11**, 418–432.

19 A. Ishikawa, T. Takata, T. Matsumura, J. N. Kondo, M. Hara, H. Kobayashi and K. Domen, Oxysulfides $Ln_2Ti_2S_2O_5$ as stable photocatalysts for water oxidation and reduction under visible-light irradiation, *J. Phys. Chem. B*, 2004, **108**, 2637–3642.

20 J. Sato, N. Saito, Y. Yamada, K. Maeda, T. Takata, J. N. Kondo, M. Hara, H. Kobayash, K. Domen and Y. Inoue, RuO_2-loaded β-Ge_3N_4 as a non-oxide photocatalyst for overall water splitting, *J. Am. Chem. Soc.*, 2005, **127**, 4150–4151.

21 K. Maeda, K. Teramura, D. Lu, T. Takata, N. Saito, Y. Inoue and K. Domen, Photocatalyst releasing hydrogen from water, *Nature*, 2006, **440**, 295.

22 B. Ohtani, Photocatalysis A to Z-What we know and what we do not know in a scientific sense, *J. Photochem. Photobiol., C*, 2010, **11**, 157–178.

23 X. Chen, S. Shen, L. Guo and S. S. Mao, Semiconductor-based photocatalytic hydrogen generation, *Chem. Rev.*, 2010, **110**, 6503–6570.

24 Q. Jing, X. Feng, X. Zhao, Z. Duan, J. Pan, L. Chen and Y. Liu, Bi/$BiVO_4$ Chain-like Hollow Microstructures: Synthesis, Characterization and Application as Visible-Light-Active Photocatalysts, *ACS Appl. Nano Mater.*, 2018, **1**, 2653–2661.

25 T. Li, L. Zhao, Y. He, J. Cai, M. Luo and J. Lin, Synthesis of g-C_3N_4/$SmVO_4$ composite photocatalyst with improved visible light photocatalytic activities in RhB degradation, *Appl. Catal., B*, 2013, **129**, 255–263.

26 T. Li, Y. Wang, Y. He, J. Cai, M. Luo and L. Zhao, Preparation and photocataytic property of $Sr_{0.25}Bi_{0.75}O_{1.36}$ photocatalyst, *Mater. Lett.*, 2012, **74**, 170–172.

27 A. Priyadharsan, V. Vasanthakumar, S. Karthikeyan, V. Raj, S. Shanavas and P. M. Anbarasan, Multi-functional properties of ternary CeO_2/SnO_2/rGO nanocomposites: Visible light driven photocatalyst and heavy metal removal, *J. Photochem. Photobiol., A*, 2017, **346**, 32–45.

28 Y. Bi, S. Ouyang, N. Umezawa, J. Cao and J. Ye, Facet effect of single-crystalline Ag_3PO_4 sub-microcrystals on photocatalytic properties, *J. Am. Chem. Soc.*, 2011, **113**, 6490–6492.

29 D. Ayodhya and G. Veerabhadram, Investigation of structural, optical, catalytic, fluorescence studies of eco-friendly synthesized Bi_2S_3 nanostructures, *Superlattices Microstruct.*, 2017, **102**, 103–118.

30 D. Ayodhya and G. Veerabhadram, One-pot green synthesis, characterization, photocatalytic, sensing and antimicrobial studies of Calotropis gigantea leaf extract capped CdS NPs, *Mater. Sci. Eng., B*, 2017, **225**, 33–44.

31 M. K. Choudhary, J. Kataria and S. Sharma, Novel Green Biomimetic Approach for Preparation of Highly Stable Au-ZnO Heterojunctions with Enhanced Photocatalytic Activity, *ACS Appl. Nano Mater.*, 2018, **1**, 1870–1878.

32 Y. Liu, Y. Jiao, Z. Zhang, F. Qu, A. Umar and X. Wu, Hierarchical SnO_2 nanostructures made of intermingled ultrathin nanosheets for environmental remediation, smart gas sensor, and supercapacitor applications, *ACS Appl. Mater. Interfaces*, 2014, **6**, 2174–2184.

33 D. Ayodhya and G. Veerabhadram, Green synthesis, optical, structural, photocatalytic, fluorescence quenching and degradation studies of ZnS nanoparticles, *J. Fluoresc.*, 2016, **26**, 2165–2175.

34 J. S. Hu, L. L. Ren, Y. G. Guo, H. P. Liang, A. M. Cao, L. J. Wan and C. L. Bai, Mass production and high photocatalytic activity of ZnS nanoporous nanoparticles, *Angew. Chem., Int. Ed.*, 2005, **117**, 1295–1299.

35 D. Ayodhya and G. Veerabhadram, Microwave-assisted synthesis, characterization and photoluminescence interaction studies of undoped, Zr^{2+}, Rh^{3+} and Pd^{2+} doped ZnS quantum dots, *Mater. Discovery*, 2018, **12**, 1–8.

36 H. C. Youn, S. Baral and J. H. Fendler, Dihexadecyl phosphate, vesicle-stabilized and in situ generated mixed cadmium sulfide and zinc sulfide semiconductor particles: preparation and utilization for photosensitized charge separation and hydrogen generation, *J. Phys. Chem.*, 1988, **92**, 6320–6327.

37 V. K. Gupta, A. Fakhri, M. Azad and S. Agarwal, Synthesis and characterization of Ag doped ZnS quantum dots for enhanced photocatalysis of Strychnine as a poison: Charge transfer behavior study by electrochemical impedance and time-resolved photoluminescence spectroscopy, *J. Colloid Interface Sci.*, 2018, **510**, 95–102.

38 A. Fkiri, A. Mezni and L. S. Smiri, Facile Synthesis of Cu Doped Au–ZnS Photocatalyst, *J. Inorg. Organomet. Polym.*, 2018, **28**, 27–34.

39 I. Tsuji, Y. Shimodaira, H. Kato, H. Kobayashi and A. Kudo, Novel stannite-type complex sulfide photocatalysts A^I_2-Zn-A^{IV}-S_4 (A^I = Cu and Ag; A^{IV} = Sn and Ge) for hydrogen evolution under visible-light irradiation, *Chem. Mater.*, 2010, **22**, 1402–1409.

40 Z. Lei, W. You, M. Liu, G. Zhou, T. Takata, M. Hara, K. Domen and C. Li, Photocatalytic water reduction under visible light on a novel $ZnIn_2S_4$ catalyst synthesized by hydrothermal method, *Chem. Commun.*, 2003, 2142–2143.

41 S. Shi, M. A. Gondal, A. A. Al-Saadi, R. Fajgar, J. Kupcik, X. Chang, K. Shen, Q. Xu and Z. S. Seddigi, Facile preparation of g-C_3N_4 modified BiOCl hybrid photocatalyst and vital role of frontier orbital energy levels of model compounds in photoactivity enhancement, *J. Colloid Interface Sci.*, 2014, **416**, 212–219.

42 Y. Wu, M. Xing, B. Tian, J. Zhang and F. Chen, Preparation of nitrogen and fluorine co-doped mesoporous TiO_2 microsphere and photodegradation of acid orange 7 under visible light, *Chem. Eng. J.*, 2010, **162**, 710–717.

43 K. Nagaveni, M. S. Hegde and G. Madras, Structure, photocatalytic activity of $Ti_{1-x}M_xO_{2\pm1}$ (M = W, V, Ce, Zr, Fe, and Cu) synthesized by solution combustion method, *J. Phys. Chem. B*, 2004, **108**, 20204–20212.

44 C. J. Xing, Y. J. Zhang, W. Yan and L. J. Guo, Band structure controlled solid solution of $Cd_{1-x}Zn_xS$ photocatalyst for hydrogen production by water splitting, *Int. J. Hydrogen Energy*, 2006, **31**, 2018–2024.

45 X. Zhao, S. Su, G. Wu, C. Li, Z. Qin, X. Lou and J. Zhou, Facile synthesis of the flower-like ternary heterostructure of Ag/ZnO encapsulating carbon spheres with enhanced photocatalytic performance, *Appl. Surf. Sci.*, 2017, **406**, 254–264.

46 C. Wang, E. Yifeng, L. Fan, S. Yang and Y. Li, CdS-Ag nanocomposite arrays: enhanced electro-chemiluminescence but quenched photoluminescence, *J. Mater. Chem.*, 2009, **19**, 3841–3846.

47 H. X. Sang, X. T. Wang, C. C. Fan and F. Wang, Enhanced photocatalytic H_2 production from glycerol solution over ZnO/ZnS core/shell nanorods prepared by a low temperature route, *Int. J. Hydrogen Energy*, 2012, **37**, 1348–1355.

48 P. Fageria, S. Gangopadhyay and S. Pande, Synthesis of ZnO/Au and ZnO/Ag nanoparticles and their photocatalytic application using UV and visible light, *RSC Adv.*, 2014, **4**, 24962–24972.

49 J. Xue, S. Ma, Y. Zhou, Z. Zhang and P. Jiang, Synthesis of Ag/ZnO/C plasmonic photocatalyst with enhanced adsorption capacity and photocatalytic activity to antibiotics, *RSC Adv.*, 2015, **5**, 18832–18840.

50 S. P. Adhikari, H. R. Pant, J. H. Kim, H. J. Kim, C. H. Park and C. S. Kim, One pot synthesis and characterization of Ag-ZnO/g-C_3N_4 photocatalyst with improved photoactivity and antibacterial properties, *Colloids Surf., A*, 2015, **482**, 477–484.

51 F. Chen, Q. Yang, Y. Zhong, H. An, J. Zhao, T. Xie, Q. Xu, X. Li, D. Wang and G. Zeng, Photo-reduction of bromate in drinking water by metallic Ag and reduced graphene oxide (RGO) jointly modified BiVO4 under visible light irradiation, *Water Res.*, 2016, **101**, 555–563.

52 F. Chen, Q. Yang, X. Li, G. Zeng, D. Wang, C. Niu, J. Zhao, H. An, T. Xie and Y. Deng, Hierarchical assembly of graphene-bridged Ag_3PO_4/Ag/$BiVO_4$ (040) Z-scheme photocatalyst: An efficient, sustainable and heterogeneous catalyst with enhanced visible-light photoactivity towards tetracycline degradation under visible light irradiation, *Appl. Catal., B*, 2017, **200**, 330–342.

53 F. Chen, Q. Yang, Y. Wang, F. Yao, Y. Ma, X. Huang, X. Li, D. Wang, G. Zeng and H. Yu, Efficient construction of bismuth vanadate-based Z-scheme photocatalyst for simultaneous Cr(VI) reduction and ciprofloxacin oxidation under visible light: Kinetics, degradation pathways and mechanism, *Chem. Eng. J.*, 2018, **348**, 157–170.

54 F. Chen, Q. Yang, S. Wang, F. Yao, J. Sun, Y. Wang, C. Zhang, X. Li, C. Niu, D. Wang and G. Zeng, Graphene oxide and carbon nitride nanosheets co-modified silver chromate nanoparticles with enhanced visible-light photoactivity and anti-photocorrosion properties towards multiple refractory pollutants degradation, *Appl. Catal., B*, 2017, **209**, 493–505.

55 D. Ayodhya and G. Veerabhadram, Highly efficient sunlight-driven photocatalytic degradation of organic pollutants and fluorescence detection of Hg^{2+} using multifunctional GO-Bi_2S_3 nanostructures, *J. Photochem. Photobiol., A*, 2018, **356**, 545–555.

56 M. Khatamian, M. S. Oskoui, M. Haghighi and M. Darbandi, Visible-light response photocatalytic water splitting over CdS/TiO_2 and CdS-TiO_2/metalosilicate composites, *Int. J. Energy Res.*, 2014, **38**, 1712–1726.

